AIP | Journal of Applied Physics

Scanning AC nanocalorimetry combined with in-situ x-ray diffraction

Kechao Xiao, John M. Gregoire, Patrick J. McCluskey, Darren Dale, and Joost J. Vlassak

Citation: J. Appl. Phys. **113**, 243501 (2013); doi: 10.1063/1.4811686
View online: http://dx.doi.org/10.1063/1.4811686
View Table of Contents: http://jap.aip.org/resource/1/JAPIAU/v113/i24
Published by the AIP Publishing LLC.

Scanning AC nanocalorimetry combined with *in-situ* x-ray diffraction

Kechao Xiao,[1,a)] John M. Gregoire,[2,a),b)] Patrick J. McCluskey,[3,b)] Darren Dale,[4] and Joost J. Vlassak[1,c)]
[1]*School of Engineering and Applied Sciences, Harvard University, 29 Oxford Street, Cambridge, Massachusetts 02138, USA*
[2]*Joint Center for Artificial Photosynthesis, California Institute of Technology, 1200 East California Blvd., Pasadena, California 91125, USA*
[3]*GE Global Research, One Research Circle, Niskayuna, New York 12309, USA*
[4]*Cornell High Energy Synchrotron Source, Ithaca, New York 14853, USA*

(Received 23 April 2013; accepted 6 June 2013; published online 24 June 2013)

Micromachined nanocalorimetry sensors have shown excellent performance for high-temperature and high-scanning rate calorimetry measurements. Here, we combine scanning AC nanocalorimetry with *in-situ* x-ray diffraction (XRD) to facilitate interpretation of the calorimetry measurements. Time-resolved XRD during *in-situ* operation of nanocalorimetry sensors using intense, high-energy synchrotron radiation allows unprecedented characterization of thermal and structural material properties. We demonstrate this experiment with detailed characterization of the melting and solidification of elemental Bi, In, and Sn thin-film samples, using heating and cooling rates up to 300 K/s. Our experiments show that the solidification process is distinctly different for each of the three samples. The experiments are performed using a combinatorial device that contains an array of individually addressable nanocalorimetry sensors. Combined with XRD, this device creates a new platform for high-throughput mapping of the composition dependence of solid-state reactions and phase transformations. © *2013 AIP Publishing LLC*.
[http://dx.doi.org/10.1063/1.4811686]

I. INTRODUCTION

Nano-calorimetry is a recently developed materials characterization technique that has advanced rapidly in recent years.[1,2] It enables ultrasensitive calorimetry measurements on very small samples of materials through use of micromachined sensors with vanishingly small thermal mass. Due to the small thermal mass of the sensors, very fast heating rates can be achieved that minimize heat loss to the environment. For instance, the nanocalorimetry sensor originally developed by Allen and coworkers can attain heating rates as large as 10^5 K/s and has been used to perform very precise heat capacity measurements on nanoparticles[3,4] and ultrathin polymer films.[5–7] Schick *et al.* have developed a different sensor that can operate under non-adiabatic conditions with controlled heating and cooling rates in the range of 10^3 K/s.[8,9] A recent development in combinatorial nanocalorimetry by McCluskey and Vlassak expands the application of nanocalorimetry to material libraries with composition gradients, enabling high-throughput analysis of complex materials systems.[10,11] This combinatorial technique can be used to study the kinetics of phase transformations and the effects of heat treatments as a function of composition and has been applied successfully to shape memory alloys and metallic glasses.[12–14]

An important challenge in the nanocalorimetric study of multi-component materials systems is to assign the features in the calorimetric trace to the various physical events that take place as a function of temperature—phase transitions in multi-component systems lead to complex calorimetric signals. One possible approach to resolve this challenge consists of simultaneously performing x-ray diffraction (XRD) and calorimetry measurements. XRD provides a wealth of structural information and allows identification of the phases present in a sample at a given temperature, while calorimetry yields thermodynamic and kinetic data that are highly temperature-resolved. In practice, combining both techniques is difficult due to the very different time scales involved in the techniques and the very small mass of the samples. For instance, to minimize heat loss, nanocalorimetry measurements are often performed at heating rates in excess of 10^3 K/s—a typical scan may last only a fraction of a second. XRD measurements, on the other hand, can require long exposure times and a typical θ-2θ scan on a thin-film sample may last hours. In this paper, we describe a new technique, where we combine scanning AC nanocalorimetry with *in-situ* XRD measurements using synchrotron radiation.

Scanning AC nanocalorimetry[15] is a calorimetry technique in which an input power oscillation is superposed on a sample during a regular scanning calorimetry measurement. The amplitude and phase lag of the resulting temperature oscillation provide accurate information on both the heat capacity of the sample and its heat loss to the environment. Using this idea, Huth *et al.*[16] and Guenther *et al.*[17] developed AC chip-calorimeters that can operate at scanning rates below 10 K/min. Xiao *et al.*[15] recently developed a different

[a)]Xiao and Gregoire contributed equally to this work.
[b)]This research was performed while the author was at the School of Engineering and Applied Sciences, Harvard University, 29 Oxford Street, Cambridge, Massachusetts 02138, USA.
[c)]E-mail address: vlassak@esag.harvard.edu

scanning AC nanocalorimetry technique that enabled measurements from nearly isothermal to rates as high as 2×10^3 K/s. This development, combined with the high intensity of a synchrotron x-ray source, has made it possible to perform *in-situ* XRD measurements during a nanocalorimetry scan.

Here, we provide a detailed description of the experimental technique and illustrate its capabilities by presenting preliminary measurements on a few simple materials systems. In Sec. II, we describe the micromachined nanocalorimetry device that was used for the measurements, and we provide a detailed account of the experimental set-up that was used to perform the XRD and calorimetry measurements at the synchrotron. In Sec. III, we briefly review the theory that underlies scanning AC nanocalorimetry and provide the equations necessary for the analysis of the calorimetry data. This section also contains the details of the data reduction schemes. Results for experiments on thin-film samples of Bi, In, and Sn are discussed in Secs. IV and V.

II. EXPERIMENTAL SETTING

A. PnSC device

The nanocalorimetry measurements in this study were performed using a parallel nano-scanning calorimeter (PnSC). The PnSC is a micromachined device described in detail elsewhere.[10,11,15] Briefly, it consists of a silicon substrate with a 5×5 array of independently controlled calorimeter sensors. Each sensor contains a tungsten four-point electrical probe that serves both as a heating element and a resistance thermometer. The tungsten probe is supported by a freestanding silicon nitride membrane and is completely encapsulated in silicon nitride. Figure 1 shows a schematic of the sensor that was used for AC calorimetry measurements in prior work.[15] In a typical calorimetry measurement, a thin-film sample is deposited in the shaded area between the two sensing leads, and an electric current is supplied through the tungsten heating element. The measured current and voltage are used to determine the power supplied to the sample, while the temperature of the sample is determined from the resistance of the heating element, which is calibrated to temperature.

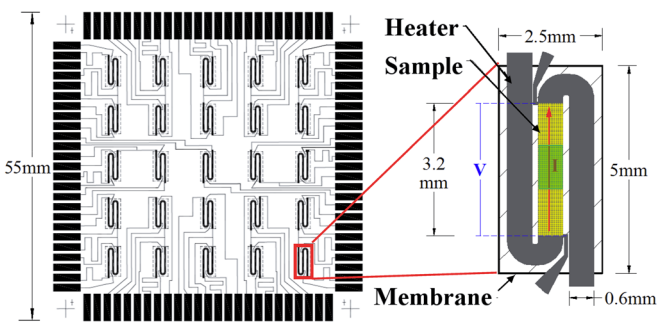

FIG. 1. Schematic of the PnSC device and calorimetry sensor. The detailed view shows the metallization within the 2.5×5 mm membrane. The sample deposition region shown in yellow is the same as the calorimeter measurement area. The subset of this area shown in green is the footprint of the x-ray beam.

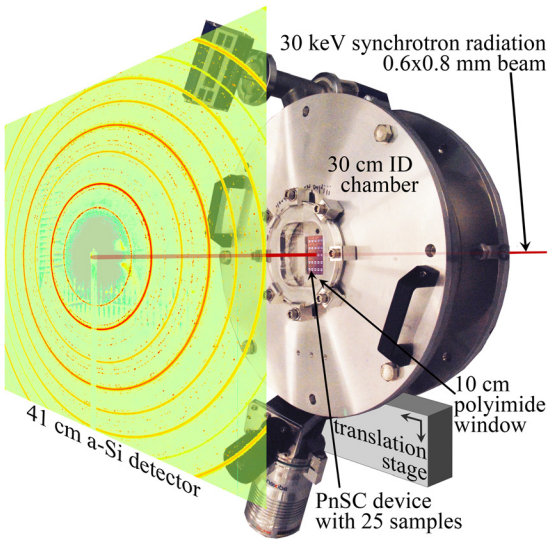

FIG. 2. Experimental set-up used for the *in-situ* diffraction and nanocalorimetry measurements. The sample is located inside the chamber; the XRD measurements are performed in transmission geometry during the nanocalorimetry scan.

B. Measurement set-up

The XRD measurements were performed at the Cornell High Energy Synchrotron Source (CHESS) using a transmission-geometry diffraction experiment (see Fig. 2), described elsewhere.[18] On the CHESS A2 beamline, a lightly sanded Si-111 double-crystal monochromator provided a 30 keV x-ray beam with a flux of 4.5×10^{10} photons per second in the 0.6×0.8 mm beam cross-section. A large-area pixel array detector (GE 41RT) optimized for efficient detection of high-energy x rays was used in transmission geometry to acquire diffraction data. The detector can image as fast as 30 frames per second.

To control the ambient atmosphere during the calorimetry measurement, the measurements were performed inside a small custom-built vacuum chamber with internal diameter of 30 cm to accommodate the probe card and PnSC device. To align the x-ray beam with each of the calorimeter samples in the 5×5 array, the entire chamber was mounted on a two-dimensional translation stage. The chamber contained an upstream x-ray window slightly larger than the PnSC device size and a considerably larger downstream window to avoid obstructing the diffraction cone from each calorimeter. Each window was custom made by sealing 0.1 mm-thick polyimide film to a flanged aluminum frame using epoxy (Varian TorrSeal). The chamber was evacuated with a compact molecular drag turbo pump (Adixen MDP-5011) backed by a rotary vane pump (Edwards RV3). The chamber pressure was measured using thermocouple and ionization vacuum gauges (Kurt J Lesker 300 and 354). The chamber was evacuated to a base pressure of 10^{-6} Torr, and measurements were performed either at this pressure or under a fixed pressure of 500–750 mTorr of helium.

C. Data acquisition system

Nanocalorimetry measurements were performed using a data acquisition system controlled with LABVIEW®, along with

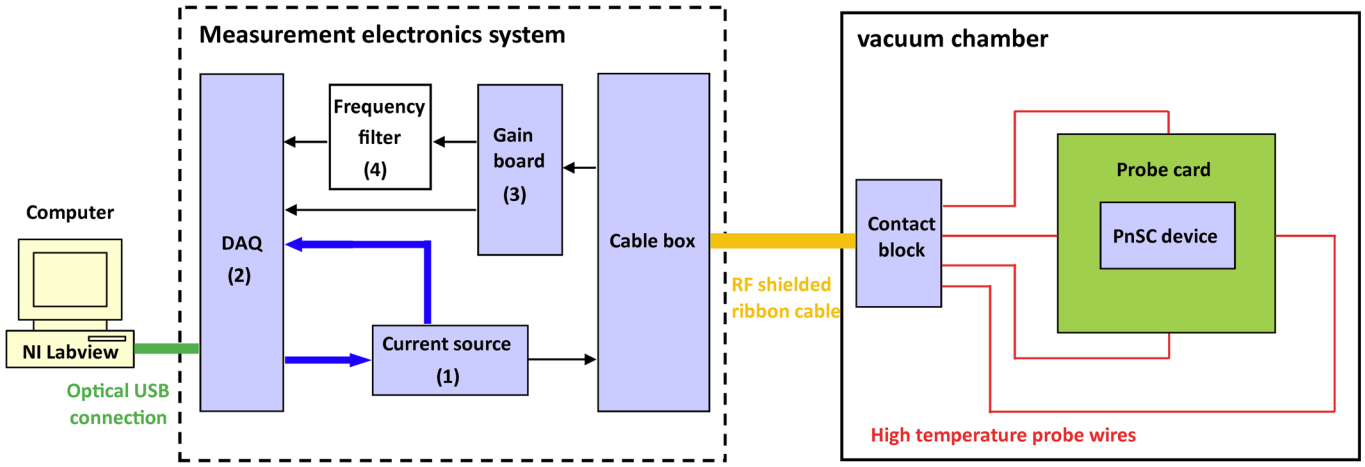

FIG. 3. Schematic of the data acquisition system.

a programmable current source. The systems consisted of several sub-systems as illustrated in Fig. 3: (1) A current source for powering the PnSC sensors and for monitoring the current output; (2) a DAQ controller for acquiring the voltage output signals from the PnSC sensors; (3) an amplifier board for conditioning of the sensor's voltage response and (4) a band pass filter (Stanford Research Systems, SR640).

The data acquisition electronics setup was similar to that described in Refs. 10 and 15, with modifications to create a compact, portable system. Computer control and measurements were performed through a digital-to-analog (DA) and analog-to-digital (AD) module (National Instruments, NI cDAQ-9174 integrated with NI 9263 and NI 9205). The modified Howland current source consisted of three high-precision, low noise operational amplifiers (OPA2227, Texas Instruments, Austin, TX), and a high-output current differential driver (AD815, Analog Devices, Norwood, MA). The current source was driven by a 100 kHz DA voltage output, providing capability for AC experiments up to 25 kHz. The applied current was determined by measuring the voltage across a precision resistor in series with the calorimeter device. The voltage across the calorimeter was measured directly, and this signal was also input into the band pass filter. The output of the band pass filter, the calorimeter voltage, and the precision resistor voltage were all sampled with the AD module, using the pseudo-differential sampling mode for noise rejection. Noise rejection was also engineered into the electronics by isolating the DAQ module and current source from earth ground, which was accomplished with low-noise and ground-isolated DC power supplies (Agilent E3630A and E3620A) as well as galvanically isolating the DAQ communications over an optically isolated Universal Serial Bus (USB) interface to the computer. One voltage probe of the 4-point calorimeter cell was earth-grounded, and ground shields for all other cables were connected at this single ground terminal. Individual sensors on the PnSC device were selected by manually switching wire connections between the probe card and the data acquisition system. The measurement system did not have any feedback loop to control the sensor temperature; experiments were performed by applying pre-defined current profiles to the sensors. The integrated measurement system was controlled via a LABVIEW® program on the user computer. For a given experiment, both the calorimetry and XRD acquisition systems were triggered with a user-activated TTL signal and ran according to a pre-defined timing schedule.

D. Sensor calibration and sample preparation

After microfabrication of the PnSC device, each sensor was calibrated by measuring the resistance of the heating element and its linear temperature coefficient. The PnSC device was placed in a vacuum furnace and the furnace temperature was stepped from room temperature to 443 K in approximately 15 K intervals. The vacuum furnace was filled with helium gas to provide temperature uniformity within the chamber. At each temperature step, a DC current of 1 mA, which yielded negligible Joule heating, was passed through each heating element on the PnSC device, and the voltage across the heating element was recorded. The resistance of the heating elements was found to increase linearly with temperature over the entire temperature range of interest, in accordance with the previously detailed calibration of the resistance thermometers.[10,11] Typical experimental values of the resistance, R_{RT}, and the thermal coefficient of resistance, λ_{RT}, at room temperature were $5.37 \pm 0.02\,\Omega$ and $(1.65 \pm 0.02) \times 10^{-3}\,\mathrm{K}^{-1}$, respectively.

Elemental Sn, Bi and In samples were deposited onto the sensors by magnetron sputtering in a centered, on-axis geometry. The depositions were performed using a shadow mask to limit deposition to the center segment of each serpentine sensor. The deposition parameters are summarized in Table I. The total deposited mass was calculated from the

TABLE I. Sample deposition parameters.

Material	Ar pressure (Pa)	Power (W)	Rate (nm/s)	Thickness (nm)	Mass (μg)
In	1.3	11	0.25	190	2.6 ± 0.4
Sn	2.4	6	0.14	100	1.4 ± 0.2
Bi	0.67	15	1.1	300	5.6 ± 0.5

mass accumulation rate, which was measured using a quartz crystal thickness monitor, and from the area of the openings in the shadow mask. The thickness values in Table I were calculated assuming standard densities of the elemental solids. After deposition, the shadow mask was removed and the samples were capped with a 32 nm aluminum nitride coating to protect the samples from the atmosphere during the calorimetry measurements. The coating was sputter deposited from an elemental Al target using a 100 kHz pulsed DC power of 89 W in a 1.25 Pa atmosphere of 20% N_2 in Ar. During this deposition, the PnSC device was rotated to attain conformal coating.

III. THEORY AND DATA REDUCTION

A. Scanning AC calorimetry

Scanning AC calorimetry measurements are performed by supplying a current

$$I = I_0 + i\cos(\omega t - \varphi_0) \tag{1}$$

to the heating element of a nanocalorimetry sensor and by measuring the corresponding 2ω voltage component across the voltage leads of the sensor (see Fig. 1). The current induces a temperature rise along with temperature oscillations of frequencies $\omega/2\pi$ and ω/π. These oscillations cause the resistance of the heating element to oscillate, which in turn causes higher harmonics in the voltage response. The 2ω voltage response of the sensor is given by[15]

$$V_{2\omega} = X_{2\omega}\cos(2\omega t) + Y_{2\omega}\sin(2\omega t), \tag{2a}$$

$$X_{2\omega} = \frac{i^2 I_0 R_0^2 \lambda}{C\omega}\left[\sin\varphi_1\cos(2\varphi_2+\varphi_1) + \frac{1}{4}\sin\varphi_2\cos(2\varphi_0+\varphi_2)\right], \tag{2b}$$

$$Y_{2\omega} = \frac{i^2 I_0 R_0^2 \lambda}{C\omega}\left[\sin\varphi_1\sin(2\varphi_2+\varphi_1) + \frac{1}{4}\sin\varphi_2\sin(2\varphi_0+\varphi_2)\right], \tag{2c}$$

where C is the total heat capacity of the heating element and sample. R_o and λ are the temperature-dependent resistance and thermal coefficient of resistance of the heating element, respectively. The phase angles φ_1 and φ_2 are related by

$$2\tan\varphi_1 = \tan\varphi_2. \tag{3}$$

Detailed derivations of Eqs. (2) and (3) can be found in our previous work.[15] When the heat loss during the calorimetry measurement is large, the phase angles approach a value of $\pi/2$, and the heat capacity C is readily determined from Eq. (2). In the Appendix, we show that C can also be determined using the following more general approach. The phase angle φ_1 is given by the following equation:

$$10\tan^3\varphi_1 + 9n\tan^2\varphi_1 + 4\tan\varphi_1 + 3n = 0, \tag{4}$$

where

$$n \triangleq \frac{X_{2\omega}\sin 2\varphi_0 - Y_{2\omega}\cos 2\varphi_0}{X_{2\omega}\cos 2\varphi_0 + Y_{2\omega}\sin 2\varphi_0}. \tag{5}$$

It can be shown that Eq. (4) has only one real root, so that $\tan\varphi_1$ is uniquely determined by Eq. (4). The total heat capacity C is then given by

$$C = \frac{i^2 I_0 {R_0}^2 \lambda}{\omega|V_{2\omega}|}\sqrt{\frac{25\tan^2\varphi_1 + 9}{16\tan^2\varphi_1 + 4}\times\frac{\tan^2\varphi_1}{1+\tan^2\varphi_1}}. \tag{6}$$

Reference 15 provides a detailed discussion on how to select the experimental parameters I_0, i, and ω to perform valid AC calorimetry measurements.

B. Data reduction for AC calorimetry measurements

To analyze the results, the measured currents and voltages for each experiment were divided into segments consisting of an integer number of AC oscillation periods. The $V_{2\omega}$ voltage was evaluated by applying a discrete Fourier transform (DFT) to every segment. All discrete Fourier transforms were performed using a second order Goertzel algorithm, which is a very efficient method of computing DFT values at specific frequencies.[19] The temperature of the sensor was calculated from the resistance of the heating element and its thermal coefficient of resistance. The total heat capacity C of a sensor with sample was calculated using Eqs. (4)–(6). Finally, a window average method was implemented to smooth the heat capacity results. All calorimetry measurements presented in this paper include the heat capacity of the addendum, which was estimated at 1.8 μJ/K from measurements performed on an empty sensor. The heat loss from sample to the environment increases with temperature and was estimated to be 40 mW at 800 K.[15]

C. XRD measurement

For each experiment, the x-ray beam was aligned to the center of the calorimeter sensor as illustrated in Fig. 1. The sample mass for the x-ray measurement was on the order of 1 μg, approximately one third of the calorimetry sample mass (see Table I). For these experiments, x-ray detector frame rates between 0.1 and 10 Hz were used for crystallographic characterization of the sample as functions of time and temperature; the acquisition times are provided in the relevant figure captions. The combination of small sample mass and short integration time pushed the detectability limit of the diffraction measurement, requiring careful data processing for quantitative analysis. The aggregate background scattering from the air, the polyimide windows, etc. was characterized by acquiring diffraction patterns on a PnSC substrate with no device. After subtracting this background and performing azimuthal integration to produce x-ray powder patterns, the sequence of patterns for a given experiment were analyzed in aggregate by summing the patterns. The Bragg peaks identified in the sum pattern were used to define segments of the powder pattern, which were analyzed in each pattern in the sequence. For each experiment, the diffraction patterns acquired near the highest sample temperature were analyzed

to confirm the absence of sample Bragg peaks, and then the average of these patterns was used as a background pattern for the sequence of images. This background subtraction method effectively removed the scattering from the tungsten heating element. Before and after each experiment, long-exposure diffraction images were also acquired to provide characterization of the room-temperature sample.

IV. RESULTS

Typical AC calorimetry results obtained for the Bi thin-film samples are shown in Fig. 4. Figure 5 shows the corresponding Bi XRD patterns obtained at different temperatures during the calorimetry scans. The heat capacity in Fig. 4 reflects the true heat capacity of the Bi sample, i.e., the energy added or extracted to reversibly heat or cool the sample without any heat loss to the environment.[15] Heating and cooling scans obtained in three different measurements are shown. The data from the three different measurements lie on top of each other, demonstrating excellent reproducibility. Both the heating scans (solid curves) and the cooling scans (dashed curves) show distinct peaks caused by melting or solidification of the sample. Unlike DC calorimetry measurements, these peaks are not directly related to the latent heat of melting.[20,21] On heating, the AC component of the power supplied to the sample during the melting process can create oscillations in the relative fraction of the two phases (i.e., movement of the phase boundary), which leads to reduced temperature oscillations and results in a distinct peak in the AC calculation of the heat capacity.[15,20] These peaks can be used to determine the melting temperature of the sample and are related to the reversibility of the reaction at the time scale of the temperature oscillation, but the area under the peak does not correspond to the latent heat of melting. The widths of the peaks are determined mainly by the temperature

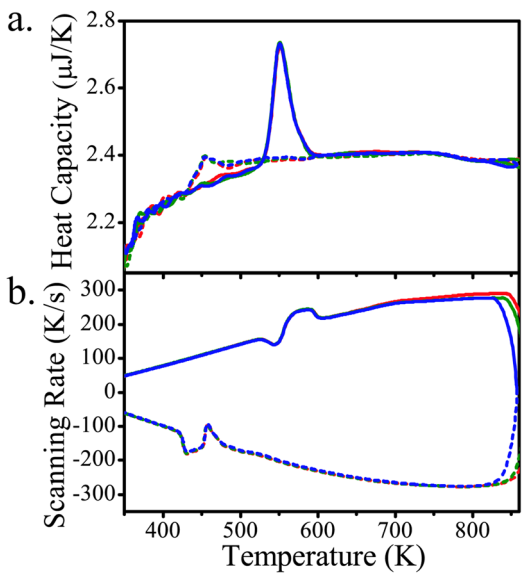

FIG. 4. (a) Heat capacity and (b) corresponding scanning rates as a function of temperature for Bi for three calorimetry scans (solid lines: heating, dashed lines: cooling). The current (I_0, i) used for the measurements was increased linearly from (20 mA, 20 mA) to (72 mA, 72 mA) and then decreased to (12 mA, 12 mA). Measurements were performed using a frequency of 416.6 Hz. The amplitude of temperature oscillation is 6.1 K at 500 K.

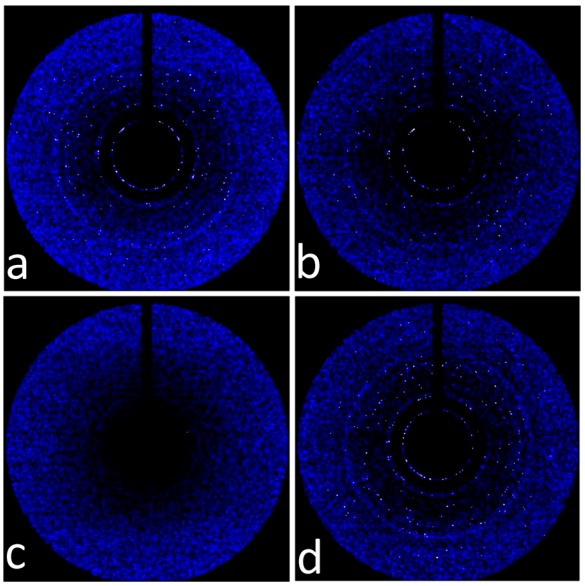

FIG. 5. XRD images taken for the Bi sample at different temperatures during the nanocalorimetry scans. (a) 373 K, (b) 473 K, (c) 673 K (above melting point), and (d) 373 K (after solidification). The XRD image acquisition time was 0.1 s.

uniformity of the sensor and the amplitude of temperature oscillation.[15] Here, the melting temperature is taken at the maximum point of the heat capacity signal.[10,15] The value for Bi is found to be 543.3 K, in good agreement with the literature value of 545.1 K.[22] The solidification peaks on cooling, however, occur at 448.7 K, which is significantly lower than the equilibrium melting temperature of Bi. The corresponding peaks in the calorimetry trace are not nearly as distinct as those on heating since the temperature oscillations are not reduced during solidification as much as they are during melting. Because of the undercooling, the solidification process is a non-equilibrium process with a rate of solidification that is set by the degree of undercooling and that has a much smaller effect on the temperature oscillations compared to melting. At temperatures between the melting and solidification points, there is a small but distinct offset between the heat capacity curves obtained on heating and cooling, indicating that the super-cooled liquid Bi has a slightly higher heat capacity than solid Bi at the same temperature. This finding is in agreement with measurements on bulk Bi samples.[23]

Figure 5 shows several Bi XRD images taken at different temperatures during the heating and cooling scans of the AC calorimetry measurement. The diffraction geometry is similar to that used in transmission electron microscopy, and the ensuing diffraction patterns, indeed, resemble those obtained in a transmission electron microscope. Due to the random crystal texture, grains diffract into Debye rings, which typically exhibit a uniform intensity distribution due to the multitude of grains in the diffracting sample volume. While the Debye rings for the metal samples contain some uniform component, samples solidified from a melt contain larger grains that produce bright spots in the Debye ring when they satisfy the Bragg condition. For the Bi sample, the images in Figure 5 show Debye rings with approximately 100 bright spots, and the same approximate number of spots

is observed in each {hkl} ring due to the random texture. Debye rings for the thinner In sample (not shown) contain only about 10 bright spots. Since the number of grains in the diffraction sample is not sufficiently large to create uniform powder diffraction rings, the use of a linear (one-dimensional) detector would fail to capture a powder pattern.

On heating, the diffraction patterns obtained at temperatures below the melting point are well matched to that of rhombohedral Bi, while those obtained above the melting point do not contain detectable Bragg peaks. On cooling below the solidification temperature, the Bi diffraction pattern reappears. The integrated diffraction intensity of the Bi {110} reflection is shown as a function of temperature in Fig. 6, clearly showing melting and solidification reactions. We also analyzed the diffraction images to ascertain the evolution of the crystal orientation distribution during the calorimetry experiment. For each image, a window of scattering vector magnitude containing the Bi {110} scattering was integrated along the scattering vector magnitude to yield the diffraction intensity as a function of detector azimuth, which is equivalent to the azimuthal orientation of the crystal grains on the sample. We quantify the evolution of this pattern as a function of temperature by calculating the correlation with the room-temperature diffraction pattern from before and after the calorimetry experiment ($C_i(T)$ and $C_f(T)$, respectively). These correlations are shown in Fig. 6 and contain three important features. First, the sharpest transitions in the correlations occur at the melting and solidification reactions as the orientation patterns of the liquid sample contain no diffraction intensity, yielding a vanishing correlation value. The most important feature of these correlations is that $C_f(T)$ is small before the melting reaction, and $C_i(T)$ is small after the solidification reaction. This observation implies that there is no measurable correlation between the orientations of the grains before and after melting, as might be the case if grains had fixed nucleation sites that would result in preferred orientations. Finally, both $C_i(T)$ and $C_f(T)$ gradually decrease from their unity value with increasing temperature. Over the temperature range of these experiments, the relative thermal expansion of the samples is on the order of 10^{-3}. The magnitudes of the scattering vectors of the Bragg peaks shift by a corresponding amount, but these shifts are not generally detected because they are much smaller than the observed peak widths and are comparable to the resolution of the diffraction measurement. Thus, thermal shifts do not contribute to the decrease in correlation with increasing temperature. Closer analysis of the orientation distribution curves (not shown) reveals that the decrease in correlation is caused by variations in the peak heights compared to the room-temperature diffraction pattern. These variations in peak heights may be caused by grain growth in the sample, which would not be surprising given the low melting point of Bi. Abrupt disappearance of a peak or appearance of a new peak, indicative of recrystallization of the sample, is not generally observed. The analysis of the structural evolution of the sample highlights the depth of information that can be obtained by combining a thin film heater/thermometer and a high-energy diffraction experiment using an area detector.

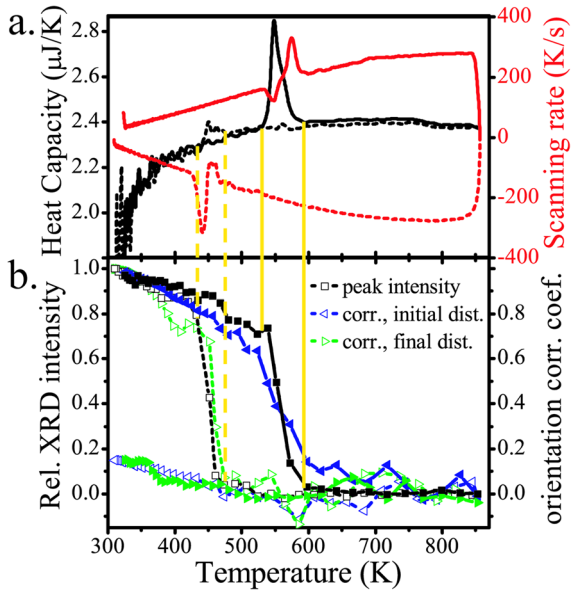

FIG. 6. (a) Heat capacity and heating rate for the Bi sample as a function of temperature, the experimental parameters are the same as in Fig. 4; (b) correlation of diffraction patterns and peak intensity as a function of temperature. Solid lines are for heating, dashed lines are for cooling. The vertical yellow lines mark alignment of the reaction windows in the PnSC and XRD signals. The image acquisition time was 0.1 s.

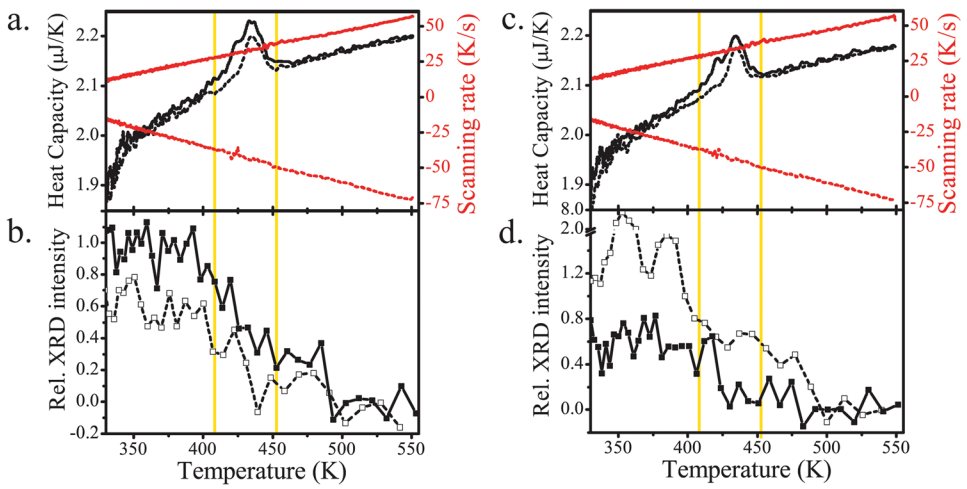

FIG. 7. Heat capacity, scanning rates, and XRD intensity for the In sample as a function of temperature for two different scans (solid lines: heating, dashed lines: cooling). (a) and (b) are results for the first measurement and (c) and (d) for second measurement. The current (I_0, i) used for the two measurements was increased linearly from (27 mA, 18 mA) to (86 mA, 59 mA) and then decreased to (13 mA, 9 mA). The AC frequency used was 416.6 Hz for both scans. The amplitude of temperature oscillation is 9.9 K at 500 K. The XRD image acquisition time was 0.1 s.

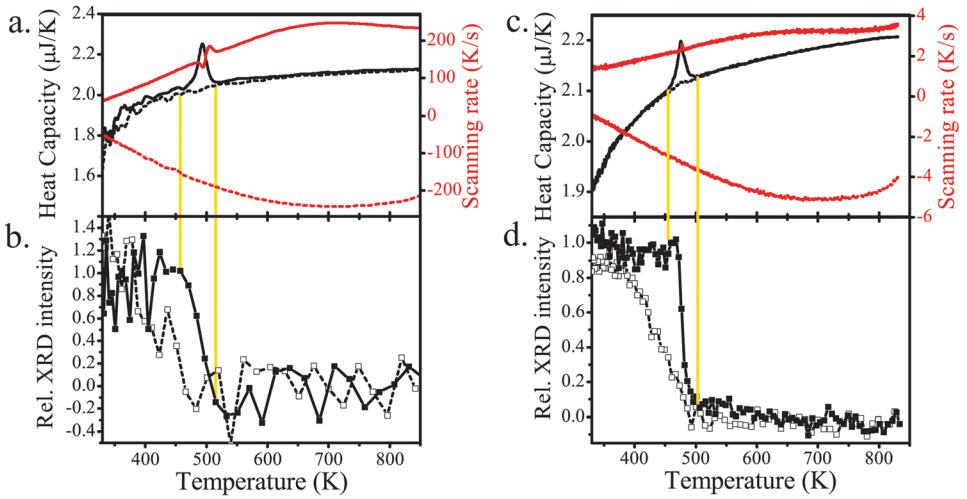

FIG. 8. Heat capacity, scanning rates and XRD intensity as a function of temperature for fast and slow scans on Sn (solid lines: heating, dashed lines: cooling). (a) and (b) are results for the fast measurement and (c) and (d) for slow measurement. The current (I_0, i) used for the fast scan was increased linearly from (20 mA, 20 mA) to (72 mA, 72 mA) and then decreased to (12 mA, 12 mA). The current (I_0, i) used for the slow scan was increased linearly from (8 mA, 8 mA) to (71 mA, 71 mA) and then decreased to (5 mA, 5 mA). The AC frequency used was 416.6 Hz for the fast scan and 99.2 Hz for the slow scan. The amplitude of temperature oscillation at 500 K is 5.9 K for fast scan and 27.7 K for slow scan. The XRD image acquisition time was 0.1 s for fast scan and 2 s for slow scan.

The AC calorimetry and XRD results obtained for the In sample are presented in Fig. 7. Results for two identical scans are shown. The calorimetry data from both measurements are nearly identical, demonstrating excellent reproducibility. Both the heating scans (solid curves) and the cooling scans (dashed curves) show distinct peaks caused by In melting and solidification, respectively. The melting temperature is found to be 432.7 K, in good agreement with the literature value of 429.7 K.[22] Unlike Bi, however, melting and solidification of In occur at the same temperatures—no undercooling is observed in Fig. 7, and the solidification proceeds in a reversible manner. As a result, the temperature oscillations are reduced both on rising and falling, and the calorimetry traces for solidification and melting are quite similar. Figure 7 also shows the intensity of the In {101} peak as a function of temperature. The change in diffraction intensity with melting and solidification is readily discerned, but compared to Bi the data are less reproducible and much noisier because of the smaller sample mass and atomic form factor of In. In the second experiment, for instance, the peak intensity briefly jumps to a very large value as a single large grain of In momentarily satisfies the Bragg condition. This phenomenon of course also occurs for Bi, but the smaller sample mass and possibly larger grains of In result in much larger statistical fluctuations.

Calorimetry and *in-situ* XRD results obtained for the Sn sample are shown in Fig. 8. The figure contains data for two sets of measurements performed at two different scan rates. The heating scans (solid curves) in the calorimetric signal show a distinct melting peak at 502.4 K for the fast scan and at 483.4 K for the slow scan. The former value agrees well with the literature value of 505 K; we attribute the offset in the slow scan to the very large temperature oscillation used in this scan (~27 K), which was an inadvertent result of the smaller AC frequency used to perform the measurement. In contrast to the heating scans, the cooling scans (dashed curves) do not have any obvious features associated with solidification. This absence of a distinct solidification peak for Sn was also observed in previous nanocalorimetry measurements.[15]

The XRD results shown in Fig. 8 were obtained using an image acquisition time of 0.1 s for the fast scan and 2 s for the slow scan—the much-improved signal-to-noise ratio for the slower scan is evident. Unlike the calorimetry traces, the XRD signals show clear transitions on both heating and cooling. The solidification process starts at the melting point and completes over a temperature range of approximately 150 K. This observation suggests a gradual solidification process in which isolated Sn droplets on the sensor solidify at different degrees of undercooling. This process is consistent with previous nanocalorimetry measurements on individual drops of Sn that showed size-dependent undercooling[24,25] in excess of 100 K. The gradual character of the solidification process explains the absence of any distinguishing features in the cooling segments of the calorimeter traces because the temperature oscillations are averaged over the entire area of the sensor.

V. DISCUSSION

The nanocalorimetry and XRD measurements on the Bi, In, and Sn samples suggest that they have rather different nucleation behavior. The Bi sample shows significant undercooling and solidifies over a narrow temperature range. The Sn sample, in contrast, starts to solidify at the melting temperature, but the process is stretched out over a broad range of temperatures. The In sample does not show any undercooling, even at cooling rates as fast as 100 K/s. The behavior of the In sample suggests that the energy barrier to nucleation of the solid phase is very small, i.e., nucleation occurs heterogeneously, and there is strong catalytic activity of either the underlying SiN_x layer or the AlN_x capping layer. The behavior of the Bi sample is more typical of a transition that occurs via a classical nucleation and growth mechanism. The undercooling is necessary to overcome the nucleation barrier, but once the solidification process starts,

it progresses quickly. The solidification of the Sn sample occurs via a similar nucleation and growth mechanism, but the gradual character of the solidification process suggests that, in this case, the film consists of individual islands with a range of sizes and with size-dependent solidification temperatures. Solidification of one island does not imply solidification of the entire film, as the islands are isolated from each other. The result is a solidification process with a temperature-dependence that is determined by the size distribution of the islands. This explanation is consistent with the microstructure of sputtered Sn films since Sn films are known to form discrete islands over a broad range of sputtering conditions[26] and the observation that melted Sn does not wet the SiN_x. Figure 9 shows an optical micrograph of a Sn sample subjected to many melting cycles. The island-structure of the sample is readily discerned. It should be noted that the size effect is a kinetic effect distinct from size-dependent melting point depression because it is observed only during solidification and not during melting.

Nucleation of a solid phase in a melt is a stochastic process. The stochastic nature can be used to obtain information on the underlying nucleation kinetics by measuring the statistical fluctuations in the undercooling. When a melt is cooled down below its melting point, the undercooling at which solidification occurs typically follows a Poisson distribution and the distribution of undercooling values, typically over a 10–20 K range,[24,27–29] can be used to derive the nucleation rate as a function of temperature.[30,31] In the present case, the Bi and In solidification peaks are highly reproducible, indicating a more deterministic solidification process. This deterministic appearance occurs because solidification of a thin-film sample is not the result of a single nucleation event, but of a very large number of events. The very large interface-to-volume ratio of a thin film provides ample opportunity for heterogeneous nucleation as confirmed by the polycrystalline structure of the samples after solidification. By contrast, many studies of metal undercooling go to great lengths to minimize nucleation through use of small spherical samples suspended in vacuum or surrounded by a flux.[24,27–29] Because so many nucleation events occur during solidification of a thin-film sample, the calorimetry trace can be regarded as a cumulative superposition of traces obtained for many individual nucleation events, and analysis of the shape of the solidification peak should provide information on nucleation statistics. There are, however, a number of other factors that influence the shape of this peak including the temperature uniformity across the sample area and the temperature oscillations of the AC measurement,[15] making the analysis somewhat involved and beyond the scope of the present manuscript. A direct comparison of the melting and the solidification peak may afford insight in nucleation statistics, provided the temperature uniformity is the same on heating and cooling. In this context, a DC calorimetry measurement would be preferred over an AC measurement because current oscillations affect the temperature of the sample differently during melting and solidification under super-cooled conditions. It is possible, however, to draw qualitative conclusions based on the calorimetry data presented above. The nucleation barrier for the In sample is very small and no undercooling is observed. The solidification and melting peaks, in this case, are determined mainly by the temperature uniformity and the AC oscillations, and indeed, they have very similar shapes. The Bi sample shows significant undercooling and analysis of the solidification peak would provide insight in the statistics of the nucleation process, at least if the effect of the AC oscillations could be eliminated. The calorimetry signal for the solidification of the Sn sample is not strong enough to allow for a meaningful analysis, but the XRD data combined with a detailed size distribution could provide information on the size-dependence of the solidification temperature.

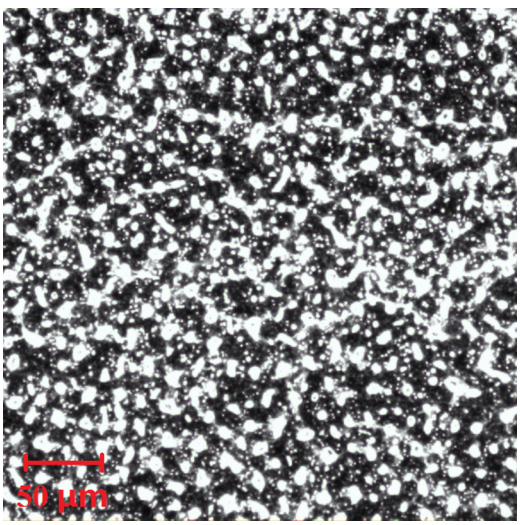

FIG. 9. Optical image of Sn sample after many melting cycles.

In-situ XRD measurements prove very useful in identifying features in the calorimetry trace such as the melting and solidification peaks in this work. Once the calorimetry features have been identified, the associated phase transformations or solid-state reactions can be investigated as a function of heating/cooling rate, heat treatment, or even composition by employing the PnSC combinatorial capability. We also note that while an inert helium atmosphere was employed in this study, the use of reactive gasses could be used to study solid-gas reactions. The large surface-to-volume ratio of the thin-film format and the ability to study thin films over a range of thicknesses will provide very high sensitivity in measurements of surface reactions. The main limitations for *in-situ* XRD measurements are currently the small masses of the samples and the very short exposure times—the scattered intensity is relatively low and requires careful analysis. This situation can be improved through use of more intense x-ray beams and faster x-ray detectors.

VI. SUMMARY

Scanning AC nanocalorimetry can be performed on thin-film samples over a wide range of scanning rates. This feature makes it possible to combine the calorimetry technique with *in-situ* X-ray diffraction measurements, allowing simultaneous structural and thermal characterization of the samples as a function of temperature. We have applied the technique to thin-film samples of Bi, In, and Sn. The melting

and solidification behavior of the samples is readily observed and our experiments show that the solidification process is distinctly different in each of the three samples.

Nanocalorimetry and *in-situ* XRD provide complementary information on the phase transformations that occur in a sample. While the application to melting and solidification of elemental metals is relatively straightforward, we anticipate that the technique will be most useful in the analysis of complex materials systems, where identification of features in the calorimetry trace is often not a trivial exercise. Combining XRD and nanocalorimetry experiments provides unprecedented capability for studying the kinetics of phase transformations or solid-state reactions and the evolution of intermediate phases.

ACKNOWLEDGMENTS

The authors thank Aaron Lyndaker for assistance with the synchrotron experiments and James MacArthur for assistance with the custom electronics. The work presented in this paper was supported by the Air Force Office of Scientific Research under Grant Nos. FA9550-08-1-0374 and FA9550-12-1-0098 and by the Materials Research Science and Engineering Center at Harvard University (NSF-DMR-0820484). The measurements were performed at the Cornell High Energy Synchrotron source (CHESS), which is supported by the National Science Foundation and the National Institutes of Health/National Institute of General Medical Sciences under NSF Award No. DMR-0936384. The sensors were fabricated at the Center for Nanoscale Systems, a member of the National Nanotechnology Infrastructure Network, which is supported by the National Science Foundation under NSF Award No. ECS-0335765. The Center for Nanoscale Systems is part of the Faculty of Arts and Sciences at Harvard University.

APPENDIX: DERIVATION OF EQUATIONS FOR THE φ_1 AND C

Dividing Eq. (2c) by Eq. (2b) and rearranging leads to

$$\sin^2\varphi_1 + n\sin\varphi_1\cos\varphi_1 + \frac{1}{4}\sin^2\varphi_2 + \frac{1}{4}n\sin\varphi_2\cos\varphi_2 = 0, \tag{A1}$$

where n is defined by Eq. (4). Since φ_1 and φ_2 are in the same quadrant, Eq. (3) implies that

$$\sin\varphi_2 = \frac{2\sin\varphi_1}{\sqrt{1+3\sin^2\varphi_1}}, \tag{A2}$$

$$\cos\varphi_2 = \frac{\cos\varphi_1}{\sqrt{1+3\sin^2\varphi_1}}. \tag{A3}$$

Substituting (A2) and (A3) into (A1) yields

$$\sin^2\varphi_1 + n\sin\varphi_1\cos\varphi_1 + \frac{\sin^2\varphi_1}{1+3\sin^2\varphi_1} + \frac{1}{2}n\frac{\sin\varphi_1\cos\varphi_1}{1+3\sin^2\varphi_1} = 0. \tag{A4}$$

Dividing this equation by $\sin\varphi_1\cos\varphi_1$ yields

$$\tan\varphi_1 + n + \frac{\tan\varphi_1}{1+3\sin^2\varphi_1} + \frac{1}{2}\frac{n}{1+3\sin^2\varphi_1} = 0. \tag{A5}$$

Substituting the relationship

$$\sin^2\varphi_1 = \frac{\tan^2\varphi_1}{1+\tan^2\varphi_1} \tag{A6}$$

into (11) finally leads to Eq. (4) presented in the manuscript.

According to the theorem of third order polynomials, Eq. (4) has only one real root uniquely defining the value of $\tan\varphi_1$. The value of $\tan\varphi_2$ can be calculated using Eq. (3).

From Eq. (2), it follows further that

$$\begin{aligned}|V_{2\omega}|^2 &= X_{2\omega}^2 + Y_{2\omega}^2 \\ &= \left(\frac{i^2 I_0 R_0^2 \lambda}{C\omega}\right)^2 \left[\sin^2\varphi_1 + \frac{1}{16}\sin^2\varphi_2 + \frac{1}{2}\sin\varphi_1\sin\varphi_2 \right. \\ &\quad \left. \times (\cos\varphi_1\cos\varphi_2 + \sin\varphi_1\sin\varphi_2)\right].\end{aligned} \tag{A7}$$

Substituting (A2), (A3), and (A6) into (A7) leads to

$$|V_{2\omega}|^2 = \left(\frac{i^2 I_0 R_0^2 \lambda}{C\omega}\right)^2 \frac{\tan^2\varphi_1}{1+\tan^2\varphi_1}\left(\frac{9+25\tan^2\varphi_1}{4+16\tan^2\varphi_1}\right), \tag{A8}$$

which finally leads to Eq. (6).

[1]S. Lai, G. Ramanath, L. Allen, P. Infante, and Z. Ma, Appl. Phys. Lett. **67**, 1229 (1995).
[2]D. Denlinger, E. Abarra, K. Allen, P. Rooney, M. Messer, S. Watson, and F. Hellman, Rev. Sci. Instrum. **65**(4), 946–959 (1994).
[3]S. L. Lai, J. Y. Guo, V. Petrova, G. Ramanath, and L. H. Allen, Phys. Rev. Lett. **77**(1), 99–102 (1996).
[4]M. Y. Efremov, F. Schiettekatte, M. Zhang, E. Olson, A. Kwan, R. Berry, and L. Allen, Phys. Rev. Lett. **85**(17), 3560–3563 (2000).
[5]M. Y. Efremov, E. A. Olson, M. Zhang, Z. Zhang, and L. H. Allen, Phys. Rev. Lett. **91**(8), 85703 (2003).
[6]M. Y. Efremov, J. Warren, E. Olson, M. Zhang, A. Kwan, and L. Allen, Macromolecules **35**(5), 1481–1483 (2002).
[7]M. Y. Efremov, E. A. Olson, M. Zhang, Z. Zhang, and L. H. Allen, Macromolecules **37**(12), 4607–4616 (2004).
[8]A. Minakov, S. Adamovsky, and C. Schick, Thermochim. Acta **432**(2), 177–185 (2005).
[9]W. Chen, D. Zhou, G. Xue, and C. Schick, Front. Chem. China **4**(3), 229–248 (2009).
[10]P. J. McCluskey and J. J. Vlassak, J. Mater. Res. **25**(11), 2086–2100 (2010).
[11]P. J. McCluskey and J. J. Vlassak, Thin Solid Films **518**(23), 7093–7106 (2010).
[12]P. J. McCluskey and J. J. Vlassak, Scr. Mater. **64**(3), 264–267 (2011).
[13]P. J. McCluskey, C. Zhao, O. Kfir, and J. J. Vlassak, Acta Mater. **59**(13), 5116–5124 (2011).
[14]J. M. Gregoire, P. J. McCluskey, D. Dale, S. Ding, J. Schroers, and J. J. Vlassak, Scr. Mater. **66**(3), 178–181 (2012).
[15]K. Xiao, J. M. Gregoire, P. J. McCluskey, and J. J. Vlassak, Rev. Sci. Instrum. **83**(11), 114901–114915 (2012).
[16]H. Huth, A. A. Minakov, and C. Schick, J. Polym. Sci., Part B: Polym. Phys. **44**(20), 2996–3005 (2006).
[17]G. Guenther, E. Aulbach, H. Hahn, and O. Guillon, Thermochim. Acta **522**(1), 77–85 (2011).
[18]J. M. Gregoire, D. Dale, A. Kazimirov, F. J. DiSalvo, and R. B. van Dover, Rev. Sci. Instrum. **80**(12), 123905–123906 (2009).
[19]G. Goertzel, Am. Math. Monthly **65**(1), 34–35 (1958).
[20]A. Lacey, D. Price, and M. Reading, *Modulated Temperature Differential Scanning Calorimetry* (2006), pp. 1–81.
[21]S. L. Simon, Thermochim. Acta **374**(1), 55–71 (2001).

[22]T. C. Totemeier and C. J. Smithells, *Smithells Metals Reference Book* (Butterworth-Heinemann, 2004).
[23]M. Kano, J. Phys. E: Sci. Instrum. **22**(11), 907 (1989).
[24]B. Yang, Y. Gao, C. Zou, Q. Zhai, A. S. Abyzov, E. Zhuravlev, J. W. P. Schmelzer, and C. Schick, Appl. Phys. A **104**(1), 189–196 (2011).
[25]B. Yang, A. Abyzov, E. Zhuravlev, Y. Gao, J. Schmelzer, and C. Schick, J. Chem. Phys. **138**, 054501 (2013).
[26]S. Hishita, Z. Stryhal, I. Sakaguchi, N. Ohashi, N. Saito, and H. Haneda, Thin Solid Films **464–465**, 146–149 (2004).
[27]G. Wilde, C. Santhaweesuk, J. Sebright, J. Bokeloh, and J. Perepezko, J. Phys.: Condens. Matter **21**(46), 464113 (2009).
[28]G. Wilde, J. Sebright, and J. Perepezko, Acta Mater. **54**(18), 4759–4769 (2006).
[29]S. Klein, D. Holland-Moritz, and D. M. Herlach, Phys. Rev. B **80**(21), 212202 (2009).
[30]M. Uttormark, J. Zanter, and J. Perepezko, J. Cryst. Growth **177**(3), 258–264 (1997).
[31]E. A. Gehan, J. Chronic Dis. **21**(9), 629 (1969).